Official Journal of CIOMP
elight.springeropen.com

RESEARCH ARTICLE

Open Access

A spatial-frequency patching metasurface enabling super-capacity perfect vector vortex beams

Zhipeng Yu[1,2,3†], Xinyue Gao[1†], Jing Yao[2,3], Zhiyuan Wang[2,3], Tianting Zhong[2,3], Yuzhi Shi[4], Bo Li[1,5], Puxiang Lai[2,3,6*], Xiangping Li[7*] and Qinghua Song[1,5*]

Abstract

Optical vortices, featured with an infinite number of orthogonal channels of orbital angular momentum, have demonstrated marvelous potentials in optical multiplexing and associated applications. However, conventional vortex beams with global phase modulation approach usually possess a single topological charge (TC) and a uniform radial distance with the donut-shaped intensity, leaving unlimited spatial intensity information unexplored. Here, to break the spatial capacity limitation, we introduce an entirely new concept of a spatial-frequency patching metasurface by patching the field distribution piece-by-piece in the spatial-frequency domain, thereby breaking the symmetry of the beam morphology and allowing for local manipulation of spatial intensity and TC distributions. Moreover, by superimposing two orthogonal circular polarized perfect VBs, our breakthrough offers a super-capacity with at least 13 channels across a 3D parametric space, including morphology, polarization azimuth and ellipticity angle, namely super-capacity perfect vector vortex beams (SC-PVVBs). Furthermore, we have designed an optimized Dammann grating to facilitate an array of SC-PVVBs, thereby unleashing the full potentials across 13 channels/bits for multi-dimensional complex information communications. Our findings promise dense data transmission in an ultra-secure manner using VBs, opening up new avenues in super-capacity optical information technology in an integrated metasurface platform.

†Zhipeng Yu and Xinyue Gao have contributed equally to this work.

*Correspondence:
Puxiang Lai
puxiang.lai@polyu.edu.hk
Xiangping Li
xiangpingli@jnu.edu.cn
Qinghua Song
song.qinghua@sz.tsinghua.edu.cn
[1] Tsinghua Shenzhen International Graduate School, Tsinghua University, Shenzhen, Guangdong, China
[2] Department of Biomedical Engineering, Hong Kong Polytechnic University, Hong Kong SAR, China
[3] Hong Kong Polytechnic University Shenzhen Research Institute, Shenzhen, Guangdong, China
[4] Institute of Precision Optical Engineering, School of Physics Science and Engineering, Tongji University, Shanghai 200092, China
[5] Suzhou Laboratory, Suzhou 215000, China
[6] Photonics Research Institute, Hong Kong Polytechnic University, Hong Kong SAR, China
[7] Guangdong Provincial Key Laboratory of Optical Fiber Sensing and Communications, Institute of Photonics Technology, Jinan University, Guangzhou 510632, China

1 Introduction

Optical vortices [1–9] have opened up a broad spectrum of applications, including particle manipulation [10–14], imaging [15, 16], holographic display [17–25], optical communication [26–28], and optical encryption [1, 29–32] due to their unique property of supporting an infinite number of orthogonal channels of orbital angular momentum. Recently, metasurfaces, comprising arrays of subwavelength structures, exhibit unparalleled ability in modulating the phase, polarization, and amplitude [33–42] of light with exceptional precision, which have been pivotal in offering a compact, efficient, and highly adaptable platform for the realization of diverse vortex beams (VBs) including simple VBs [43, 44], vector vortex beams (VVBs) [45–47], perfect vortex beam (PVBs) [48–52] and perfect vector vortex beams (PVVBs) [1, 2, 4, 53]. Conventionally, the optical field of a VB in the far

field undergoes an inverse Fourier transform as a whole to obtain the electric field in the metasurface plane. Subsequently, the required phase profile of the metasurafce is globally matched with this electric field. However, such a global phase modulation approach restricts a VB to possess only one topological charge (TC), resulting in a symmetric and uniform intensity distribution around its phase singularities [47]. Despite its potential to incorporate other optical degrees of freedom, such as polarization as shown in Fig. 1a, to enhance information capacity, the unlimited spatial intensity information remains unexplored.

In this study, we propose a general method using spatial-frequency patching metasurfaces to create a new type of VB named super-capacity perfect vector vortex beam (SC-PVVB), significantly enhancing the local modulation capacity as shown in Fig. 1b. The spatial-frequency patching, including mathematically breaking an irregularly seamless curve into a sum of several elliptic arcs in the far field and applying desired spatial-frequency profiles on each partial region in the near field, results in the formation of a super-capacity perfect vortex beam (SC-PVB) that exhibits locally controllable morphology and TC. Through the superposition of two orthogonal circular polarized SC-PVBs by leveraging a non-interleaved method [46], a single geometric metasurface is employed as an efficient, versatile and compact platform for the broadband generation of SC-PVVBs in the visible. This platform allows for extra local modulation of amplitude in each circular polarized SC-PVB, thereby extending the local modulation capacities into three dimensions, encompassing morphology, TC, and amplitude. The latter two are associated with the polarization azimuth and ellipticity angles. Here, our proposed method encompasses a super capacity of at least 13 channels across three dimensions in one SC-PVVB: morphology (5 channels), polarization azimuth (4 channels), and polarization ellipticity (4 channels), as depicted in Fig. 1c. To harness the full potential of the SC-PVVB, we have engineered an optimized Dammann grating capable of supporting a distinct SC-PVVB in every diffraction order. Consequently, within a 3*6 array of Dammann gratings, it is designed to transmit multiple pixelated characters-ranging from "0" to "9" and including "A" and "B"-simultaneously. Each character is encrypted into a specific channel with one channel in the dimension of morphology carrying a blank content. Such a scheme enables receivers to easily and reliably retrieve optical vector fields over a broadband spectrum while ensuring ultra-high security during data transmission. This research advances the state-of-the-art in VB manipulation by leveraging locally controllable capacity of VBs to broaden the potential applications across various fields such as light-matter interactions, optical encryption, high-density data communication, and particle manipulation, which will mark a significant step forward in the versatility and utility of VBs.

2 Results

Our methodological approach begins with a comparative analysis of existing work and our findings, as depicted in Fig. 1a, b. A VVB is composed of two VBs, one with right circular polarization (RCP) and the other with left circular polarization (LCP). In Fig. 1a, the phase profile of a VB is overlaid with the phase profile of an axicon for each circular polarization. This results in a PVVB with a circular ring in the Fourier plane, which is distinguished by the invariant annular intensity profile regardless of diverse TCs, exhibiting space-variant polarization azimuth and ellipticity angle. However, the TC and ring morphology can only be globally controlled, indicating limited modulation channels (Detailed discussion can be found in Supplementary Note 1). In contrast, Fig. 1b illustrates the creation of a SC-PVVB superposed with two orthogonally circular polarized SC-PVBs (whose process will be elaborated in Fig. 2) with different angular-variant morphology by breaking an irregularly seamless curve into a sum of several elliptic arcs with a spatial-frequency patching metasurface. As a result, the morphology, polarization azimuth and ellipticity angle of a SC-PVVB can be locally modulated in the Fourier plane.

As a proof of concept, we employ a single geometric metasurface utilizing a non-interleaved approach as shown in Fig. 1c, allowing for opposite geometry phases imposed in the two CP waves. Each CP beam can be independently controlled in terms of morphology, TC and amplitude for the generation of SC-PVBs. When illuminated with a linearly polarized (LP) beam, the two SC-PVBs with opposing CP states exhibit a coherent superposition, resulting in a SC-PVVB. The phase profile necessary to achieve this pair of SC-PVVBs can be mathematically described as follows:

$$\phi_{SC-PVVB} = \arg\left(E_{R\_\theta} e^{i\alpha} e^{i\phi_{SC-PVB\_R}} + E_{L\_\theta} e^{-i\alpha} e^{-i\phi_{SC-PVB\_L}}\right) \tag{1}$$

where α is the phase difference between neighboring pixels that causes a phase gradient to deflect the generated SC-PVVB. $\theta \in (0,2\pi]$ is the radial angle. The function arg() represents the phase of the optical complex field. E_{R_θ} and E_{L_θ} are amplitudes of the optical complex field of RCP and LCP with angular-variant values. ϕ_{SC-PVB_R} and ϕ_{SC-PVB_L} are required phase profiles of two circularly polarized SC-PVBs with RCP and LCP, respectively. The morphology, polarization azimuth angle ($0 \le \psi \le \pi$), and ellipticity angle ($-\pi/4 \le \chi \le \pi/4$) of the SC-PVVB can

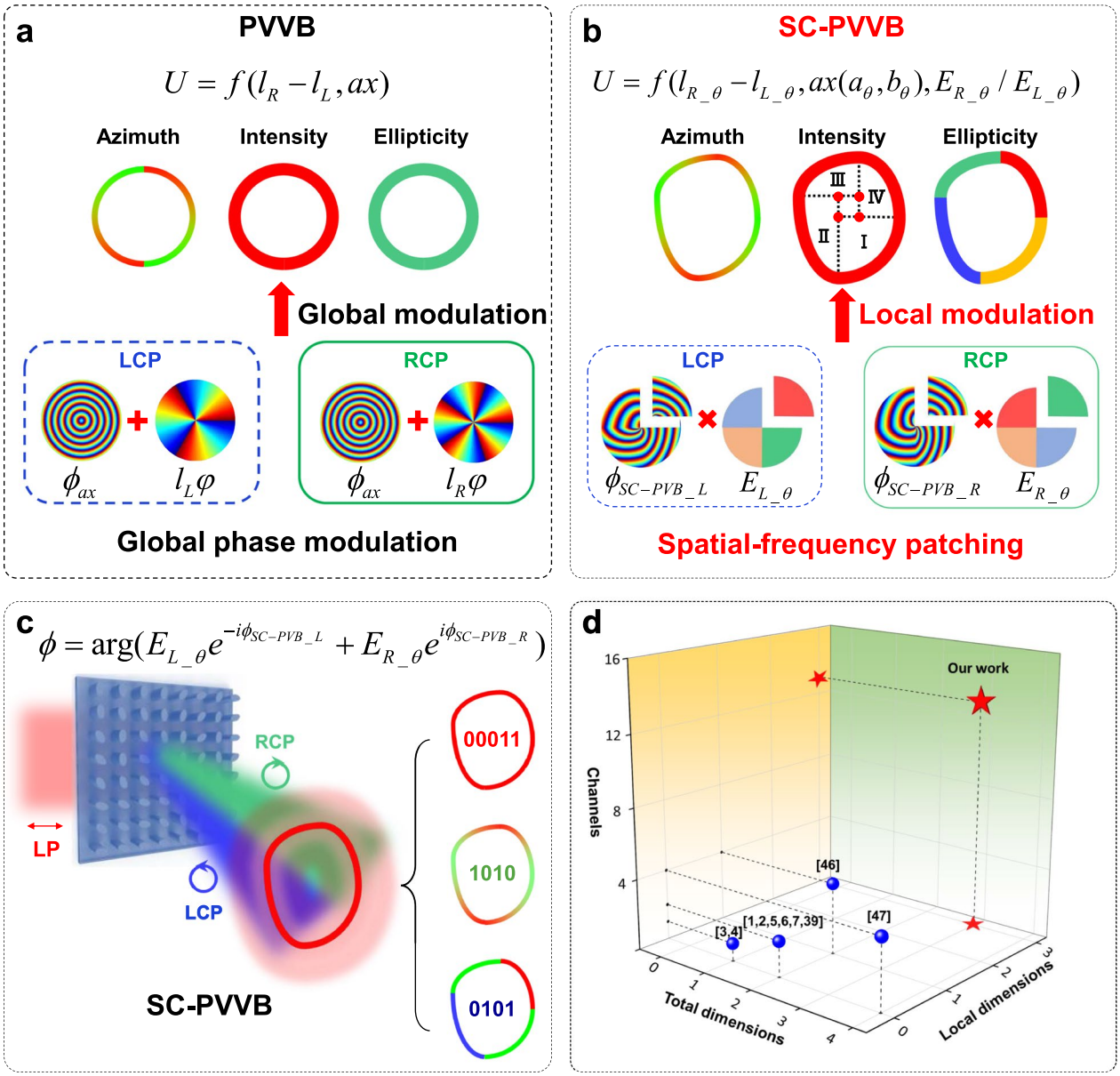

Fig. 1 Schematic diagram of the SC-PVVB. A comparison between **a** PVVB and **b** SC-PVVB. Each red spot indicates the center of one ellipse arc in the corresponding region. **c** A single geometric metasurface is used to form SC-PVVB with multidimensional modulation ability for optical encryption. **d** A comparison between the PVVBs of existing works and our method in terms of local and total dimensions, and channels. *U* is the optical field of PVVBs in the Fourier plane, which is the function (denoted as *f*) of adjustable parameters in each case. θ is the radial angle

be independently and locally manipulated to support a capacity of 13 channels. Consequently, a 13-bit digit can be encrypted or transmitted assuming each channel is taken a binary value, as shown in Fig. 1c. To provide a more intuitively comparison, the local and total dimensions and channels of existing works and our approach are presented in Fig. 1d [1–7, 46, 53, 54]. Our proposed method, denoted by a red star, offers three local modulation dimensions in morphology, polarization azimuth and ellipticity angle, along with a capacity of 13 channels. This illustrates a significant enhancement in local and total dimensions, and channels compared to other existing methods.

The process of generating a SC-PVB with a spatial frequency patching metasurface is shown in Fig. 2. It is worth noting that our approach allows for segmenting the irregularly seamless ring into an unlimited number of elliptic arcs. As a proof of concept, four quarter

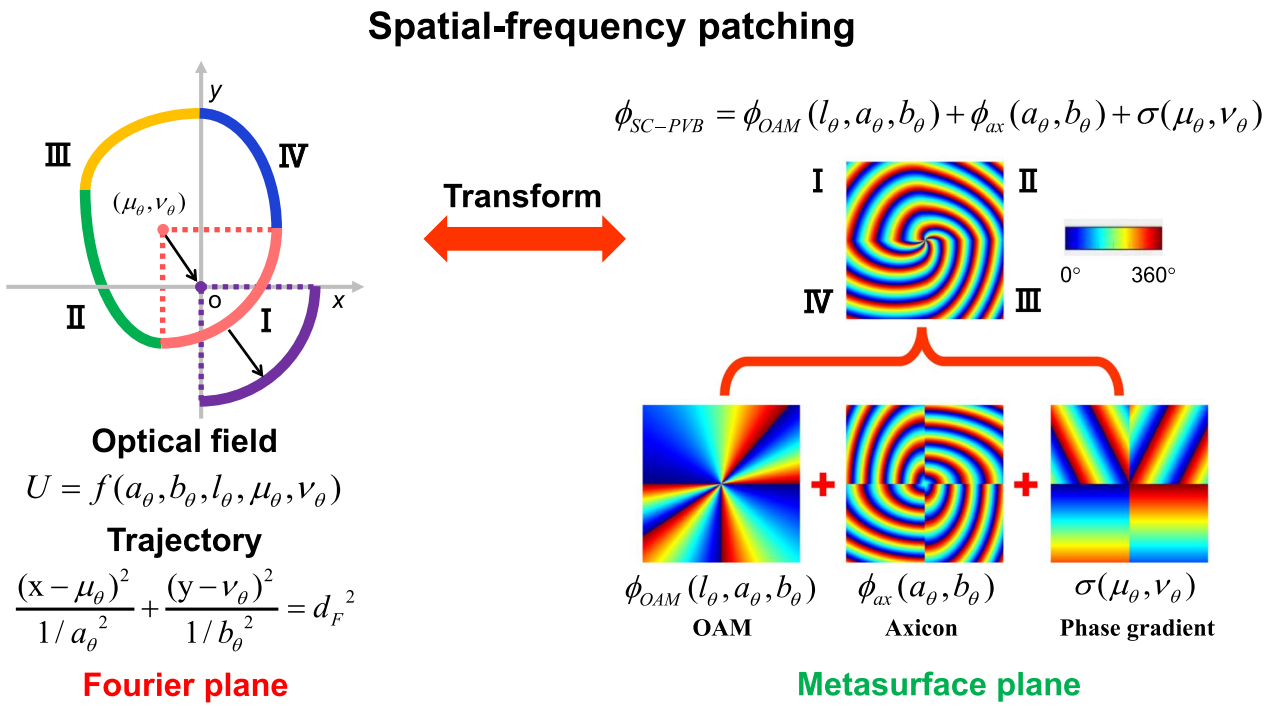

Fig. 2 Schematic diagram of the SC-PVB with spatial-frequency patching. The spatial-frequency patching process of the SC-PVB in the Fourier plane and the metasurface plane. d_F is the range scaling factor and corresponds to the axicon period

elliptic arcs (segments) forming a seamless ring serves as an example in the following discussion and experiment. Initially, in the Fourier plane, a seamless ring is mathematically analyzed to consist of four quarter elliptic arcs, with each corresponding to a unique partial ellipse PVB denoted by different colors (labeled as I, II, III, and IV). The phase profiles for VB(ϕ_{OAM}) and axicons (ϕ_{ax}) of an ellipse PVB in the polar coordinate can be mathematically represented as follows:

$$\begin{aligned} \phi_{OAM}(l,a,b) &= l \cdot \arctan\left(\frac{a}{b}\tan(\theta)\right); \\ \phi_{ax}(a,b) &= \frac{-2\pi}{d}\sqrt{\frac{(r\cos(\theta))^2}{a^2} + \frac{(r\sin(\theta))^2}{b^2}} \end{aligned} \tag{2}$$

where a and b are the horizontal and vertical normalizing factors, l is the TC, d is the axicon period to control the radius of the ring, and $r \in [0, \infty)$ is the radial distance. The center of a complete ellipse PVB coincides with the origin (o) of x-axis and y-axis. As shown in the Fourier plane in Fig. 2, the center of Segment I is marked as a red spot with a coordinate value (μ_θ, ν_θ) which can be easily coincided with the origin by moving Segment I along the black arrowed line. Such a procedure can be easily implemented by applying a phase gradient $(\sigma(\mu_\theta, \nu_\theta))$ in the metasurface plane. As a result, the phase profile in the metasurface plane corresponding to Segment I is the superposition of the phase profile of a quarter ellipse PVB and a phase gradient profile. Phase profiles of other segments can be also calculated with the same method, as shown in the metasurface plane in Fig. 2. Finally, all partial fields can be patched one-by-one to form a complete one. The phase profile of the resulting SC-PVB can be expressed as:

$$\phi_{SC-PVB} = \phi_{OAM}(l_\theta, a_\theta, b_\theta) + \phi_{ax}(a_\theta, b_\theta) + \sigma(\mu_\theta, \nu_\theta) \tag{3}$$

As shown in Fig. 2, the SC-PVB has locally controlled TCs and morphology with the proposed spatial-frequency patching metasurface. In such a case, the equivalent TC of SC-PVB with four quarter elliptic arcs could be given by $l_{SC} = \frac{l_1+l_2+l_3+l_4}{4}$, where l_n $(n=1,2,3,4)$ corresponds to the TC of the corresponding segment. As shown in Fig. 2, the simulated phase profile of the SC-PVB exhibits an equivalent TC of 5, with each segment carrying a TC of 2, 6, 4, and 8, respectively. To ensure a smooth ring without any discontinuities, parameters in Eq. (3) should adhere to strict criteria, which can be found in Supplementary Note 2.

For better visualization, b_1 is set to equal to b_2 and b_3 is also set to equal to b_4 in the following discussion and experiments, in which the junction of Segments I and IV and that of Segments II and III are aligned horizontally. According to Eqs. (1 and 3), regarding the morphology aspect, five parameters $(a_1, a_3, b_1, b_3, \frac{2}{1/a_1+1/a_2})$ can be modulated to create a closed ring. In terms of TCs, a total

of eight parameters can be manipulated. Specifically, four parameters within SC-PVB_L ($l_{1L}, l_{2L}, l_{3L}, l_{4L}$) and the other four parameters of its counterpart SC-PVB_R ($l_{1L}, l_{2L}, l_{3L}, l_{4L}$) can be adjusted. These adjustments alter the polarization order, which is related to the polarization azimuth angle within each segment of the SC-PVB. The polarization order is expressed as $(l_{nR} - l_{nL})/4$. The sign of the polarization order correlates with the rotation direction of the lobes, as indicated by the distribution of the polarization azimuth angles. A clockwise rotation of the lobes corresponds to a positive polarization order with a positive sign, while a counterclockwise rotation corresponds to a negative sign. The absolute value of the polarization order represents the number of lobes. As depicted in Fig. 1d, the rotation direction of the lobes within each segment can be manipulated to proceed either clockwise or counterclockwise. In the amplitude dimension, eight parameters can be also adjusted to modify the polarization ellipticity of each segment within the SC-PVVB. This includes four parameters for the SC-PVB_L, denoted as $(E_{1L}, E_{2L}, E_{3L}, E_{4L})$, and the corresponding four parameters for SC-PVB_R, denoted as $(E_{1R}, E_{2R}, E_{3R}, E_{4R})$. The ellipticity angle of the polarization is determined by the ratio E_{nR}/E_{nL}. Collectively, a SC-PVVB can support a capacity of 13 channels across three dimensions by measuring the polarization and intensity distributions, as summarized in Table 1.

The geometric metasurface is composed of elliptical titanium dioxide (TiO_2) meta-pillars, which are arranged on a glass (SiO_2) substrate with spatially varying orientations, as depicted in Fig. 3a. These meta-pillars have a height (h) of 600 nm and are arranged by square lattice with a periodic constant (P) of 300 nm. The meta-pillar, characterized by axis lengths of 100 nm and 260 nm, is designed as a half wave-plate to convert the spin of the two CP beams. The CP conversion efficiency of this meta-pillar as a function of wavelength, simulated using the commercial software COMSOL, is represented by the red line in Fig. 3b, in which a remarkable efficiency across a wide spectral range is achieved, particularly from 450 to 650 nm. The meta-pillar is rotated with a rotation angle of δ that is able to perform CP conversion $|L\rangle \rightarrow e^{i2\delta}|R\rangle$ and $|R\rangle \rightarrow e^{-i2\delta}|L\rangle$, *i.e.*, the LCP and RCP beams are converted to the opposite spin with a geometric phase (or Pancharatnam-Berry (PB) phase) of 2δ and -2δ, respectively, which agrees with the simulated results as shown in the blue line in Fig. 3b. Consequently, the two-dimensional rotation angle profile (ϕ_δ) of the metasurface required to construct a SC-PVVB can be derived as:

$$\phi_\delta = \frac{1}{2}(\varphi_{SC-PVVB} - \beta) \tag{4}$$

Table 1 Summary of capacity of a SC-PVVB

Dimensions	Associated parameters	Channels
Morphology	a1, a3, b1, b3, $\frac{2}{1/a_1+1/a_2}$	5
Azimuth	$\frac{l_{1R}-l_{1L}}{4}$, $\frac{l_{2R}-l_{2L}}{4}$, $\frac{l_{3R}-l_{3L}}{4}$, $\frac{l_{4R}-l_{4L}}{4}$	4
Ellipticity	$\frac{E_{1R}}{E_{1L}}$, $\frac{E_{2R}}{E_{2L}}$, $\frac{E_{3R}}{E_{3L}}$, $\frac{E_{4R}}{E_{4L}}$	4

where β is the propagation phase of the meta-pillar, which is constant for all meta-pillars due to their uniform size. Therefore, by rotating the meta-pillars, a pure geometric phase can be obtained. For simplicity, we ignore the propagation phase and set it as β=0°. A designed rotation angle profile (only 200*200 pixels in the central region are displayed for better visualization) for one sample in the following experiment is shown in Fig. 3c. Scanning electron microscope (SEM) images depicting the top view of the fabricated metasurface are presented in Fig. 3d (see more fabrication details in Methods section).

The experimental optical setup for the metasurface is illustrated in Fig. 4a (see more details in Methods). The measured results are shown in Fig. 4b–d, where we demonstrate three distinct configurations of SC-PVVBs consisting of two, three, and four partial elliptic arcs. Figure 4b illustrates a SC-PVVB of consisting four partial elliptic arcs at the wavelength of 532 nm, labeled as segments I, II, III, and IV in the intensity profile (first column). The axicon period is set to 3 μm. The designed aspect ratios for the vertical and horizontal axes of these segments are 1, 0.6, 0.83, and 1.18, respectively. The measured aspect ratios in these four segments agree well with the designed values, where these ratios are approximately 1, 0.57, 0.82, and 1.18, respectively, with minor discrepancies observed in segments II and III. To assess the polarization properties, a polarizer is placed before the camera for analysis. The second and third columns present the measured intensity profiles with the polarizer axis orientations setting as 0° and 90°, respectively, revealing complementary patterns due to the orthogonality of x- and y-polarizations. TCs of 2, 2, 6 and 6 in SC-PVB_L and that of 10,10,10 and 10 in SC-PVB_R are designed in segments I, II, III, and IV, respectively, and the corresponding designed polarization orders are 2, 2, 1 and 1. The polarization azimuth and ellipticity angle of the SC-PVVB are measured through Stokes parameter measurements, as shown in the fourth and fifth columns. The measured polarization orders for these segments are 2, 2, 1, and 1, which agree with designed ones, and the polarization states (polarization ellipticity angles) are linear (~0°), left elliptical (~-20°), linear (~0°), and right elliptical (~20°), respectively. As illustrated, the polarization azimuth angle within each segment demonstrates a rigorously periodic variation. In contrast,

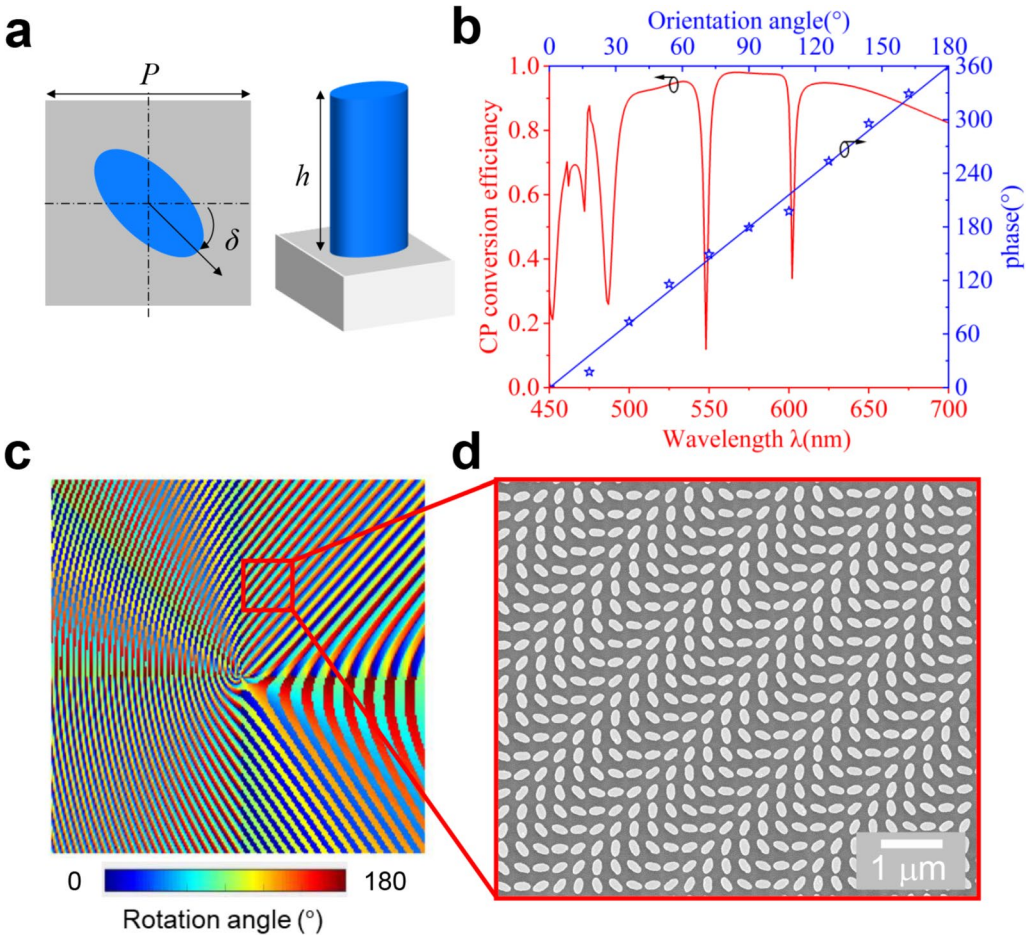

Fig. 3 Metasurface structure design and fabrication results. **a** Top and perspective views of one unit cell of the metasurface. A TiO_2 meta-pillar is arrayed in a square lattice on a fused silica substrate. **b** Simulated conversion efficiency of the meta-pillar across the 450–700 nm wavelength range (red line), and the simulated geometric phase plotted against the rotation angle of the meta-pillar (blue stars) which agrees well to the theoretical geometric phase (blue line). **c** The simulated rotation angle profile of the meta-pillar on the metasurface to generate the SC-PVVB. **d** The top view of the SEM images of the fabricated metasurface

the polarization ellipticity angle exhibits minor fluctuations indicated by the distinct color markings. The slight discrepancies and fluctuations are likely attributed to imperfections in the fabricated structures. These results indicate that the morphology, the polarization azimuth and ellipticity angle of a SC-PVVB can be locally controlled. It is noteworthy that the polarization orders of adjacent segments can have opposite signs, as evidenced in Fig. 5. The experimental evidences for these other two configurations are presented in Fig. 4c and d, showing a phenomenon consistent with that observed in Fig. 4b. A comprehensive summary of experiment results and associated parameters can be found in the Supplementary Note 3. The experimental outcomes for the SC-PVVB at the other two wavelengths of 460 nm and 650 nm to verify the broadband feature of the proposed method in the visible range can be found in the Supplementary Note 4. The SC-PVVB can also propagate robust in free space, and related results can be found in Supplementary Note 5.

Assuming each channel is encoded with binary values, the SC-PVVB can generate 2^{13} possible combinations across its modulation dimensions, including morphology, polarization azimuth and ellipticity angle. This super capacity enables a wide range of applications, such as optical encryption, information transmission and communication. In our proof-of-concept demonstration, we propose a multi-dimensional information transmission scheme with the assist of an optimized Dammann grating, as shown in Fig. 5. By incorporating an optimized phase shift into each diffraction order of the Dammann grating, the optical field for each order can be independently designed using phase-only modulation. The requisite phase profile for each order of grating is refined

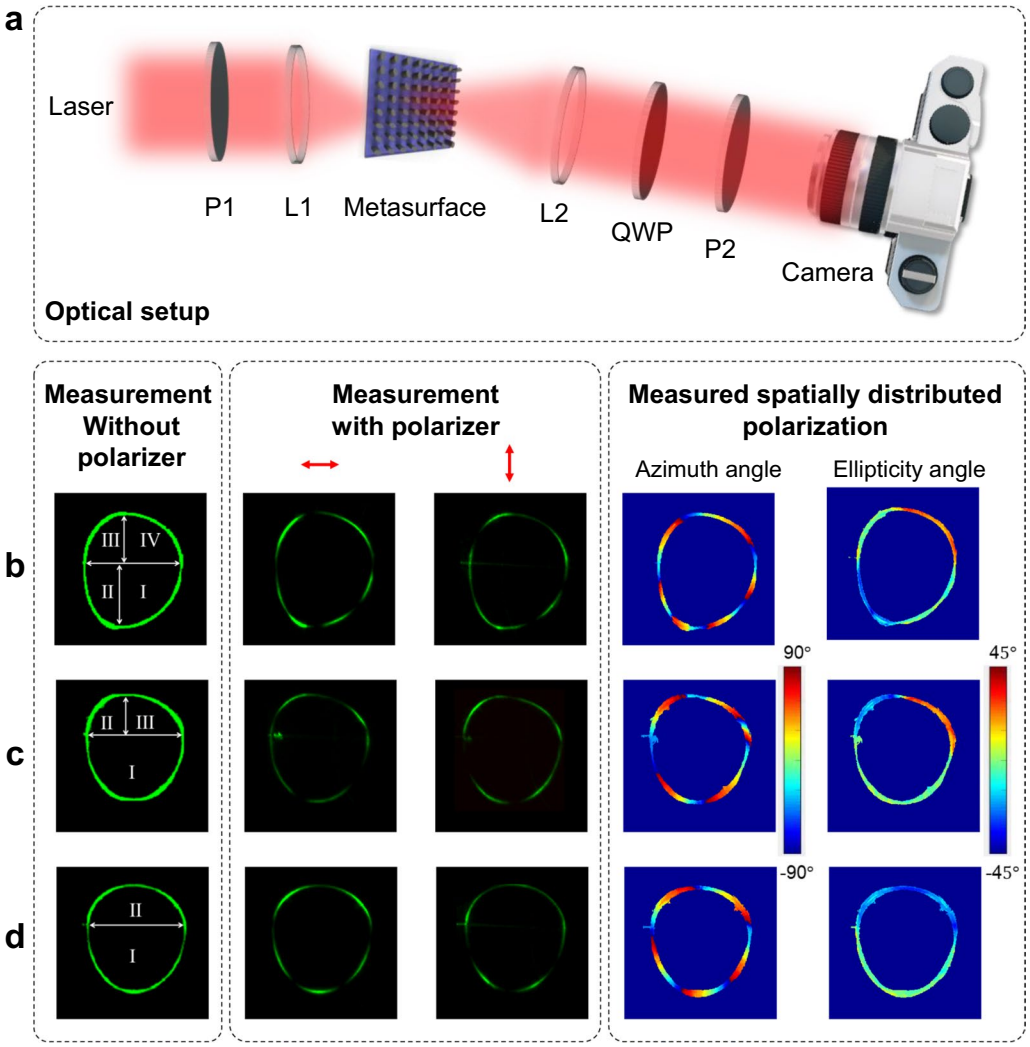

Fig. 4 The experimental optical setup and measurement results of the metasurface. **a** Experimental diagram of the optical setup for the measurement of SC-PVVB. **b** Four independent segments. **c** Three independent segments. **d** Two independent segments. P1–P2: linear polarizer; L1–L2: lens; QWP: quarter-wave plate; sCMOS: scientific complementary metal–oxide–semiconductor

through optimization with a genetic algorithm, as discussed in detail in Supplementary Note 6.

As depicted in Fig. 5a, Alice has constructed a lookup table containing 16 combinations, with each combination corresponding to a unique 4-bit digit in each dimension. This table is utilized to illustrate the encryption rule for each channel. What should be noticed is that the parameter $2/(1/a_1 + 1/a_2)$ is a constant in all combinations to ensure a same number of combinations in each dimension for simplification. For the shape dimension, the binary value is determined by the parameter value (a_1, a_3, b_1, b_3): a higher parameter value corresponding to a shorter axis length yields a binary "1", otherwise a binary "0" is yielded. 16 SC-PVVBs with diverse shapes can be observed with each encoded with a 4-bit digit. For the ellipticity angle dimension, the binary value is determined by the parameter values $(\frac{E_{nR}}{E_{nL}}, n = 1,2,3,4)$: a value of the ellipticity angle greater than 0° results in a binary "1", and that smaller than 0° generates a binary "0". In the azimuth angle dimension, the binary value is determined by the value of the TC difference between the SC-PVBs in RCP and LCP $(\frac{l_{nR}-l_{nL}}{4}(i = 1,2,3,4))$: a value of 1 consistent with a polarization order (clockwise rotation) of 1 leads to a binary "0", and a value of − 1 consistent with a polarization order of − 1 (anticlockwise rotation) leads to a binary "1". According to the lookup table and utilizing an inverse design methodology detailed in this work, a metasurface with engineered 2-D structures with customized information in each channel will be fabricated by Alice. Bob (Receiver) begins by measuring the optical

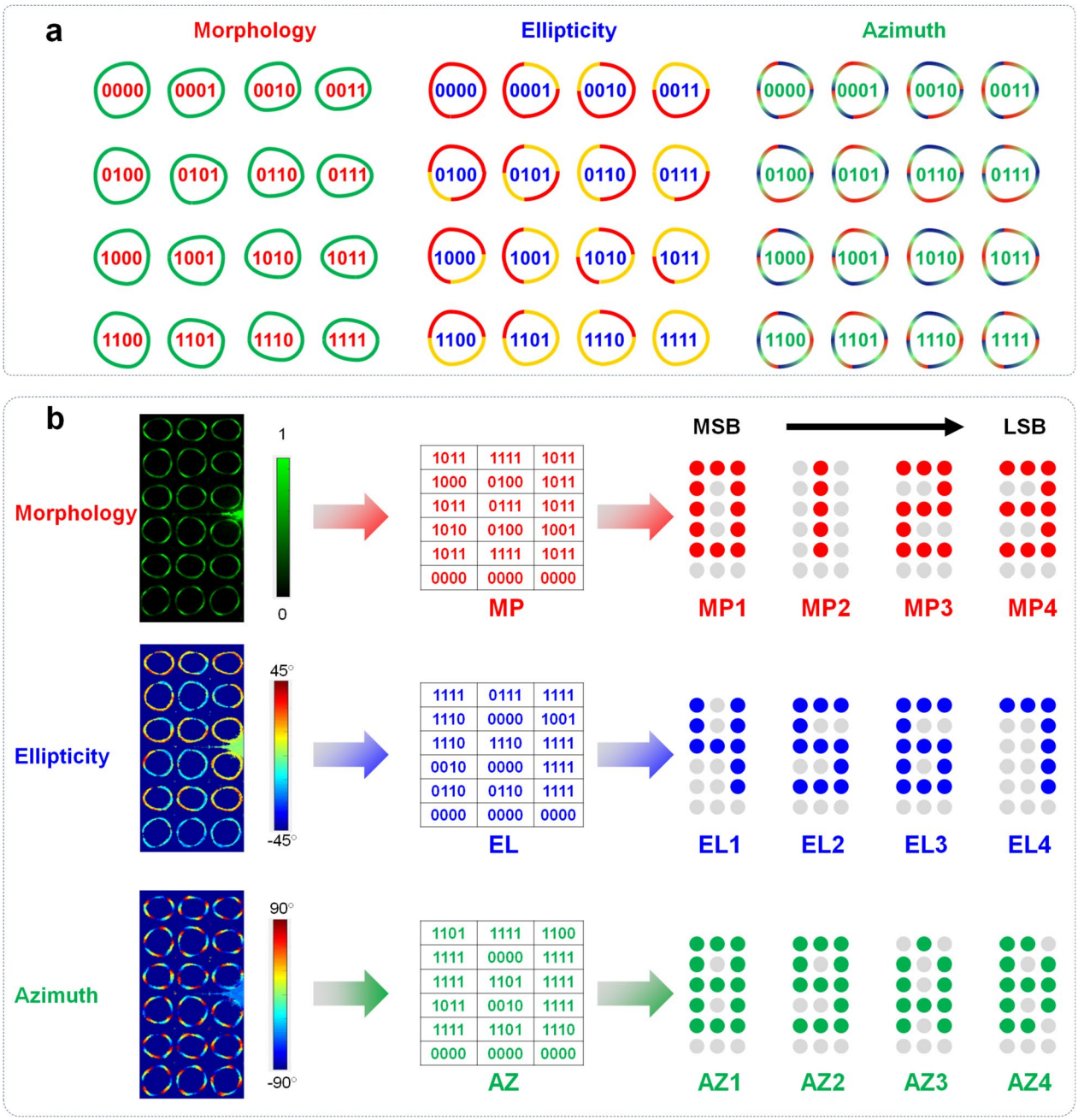

Fig. 5 Multi-dimensional information transmission with an array of distinct SC-PVVBs. **a** A lookup table containing three arrays with each encoded with a distinct 4-bit digit across three dimensions. **b** Detection of the optical output field containing a 3 × 6 array of distinct SC-PVVB and the decryption process of multi-dimensional information from the optical field. LSB: least significant bit; MSB: most significant bit

output field of the metasurface with a linearly polarized light beam. As shown, a 3 × 6 array of SC-PVVBs (only left half part of the optical field is shown and it is discussed in detail in Supplementary Note 6) with specific distribution in each channel can be detected. When Bob analyzes the optical vector field, he must adhere to the rules specified in the lookup table authorized from Alice. By adhering strictly to these rules, Bob can decode three 3*6 arrays, each containing a 4-bit digit in every element. Each array corresponds to an individual dimension and is labeled as "MP", "EL", and "AZ". Within each element, the bits are sequentially numbered from 1 to 4, starting with the most significant bit (MSB) and ending with the least significant bit (LSB). Furthermore, twelve 3*6 arrays, each with a binary digit in every element, can be derived by extracting individual bits from the digits in "MP", "EL",

and "AZ". These arrays correspond to each channel with four arrays per dimension. The last rows of these three arrays each have their three digits set to "0000", serving as a reference for orientation. Ultimately, Bob can decrypt the customized information sent by Alice. As an illustration, the array "MP" includes four pixelated characters "0", "1", "2", and "3", which are designated as "MP1", "MP2", "MP3", and "MP4", respectively. Similarly, the array "EL" contains the characters "4", "5", "6", and "7", marked as "EL1", "EL2", "EL3", and "EL4", respectively. Lastly, the array "AZ" comprises the characters "8", "9", "A", and "B", labeled as "AZ1", "AZ2", "AZ3", and "AZ4", respectively. One SC-PVVB (located in column 2, row 5) exhibits some minor fluctuations in the ellipticity angle. In the upper right part of the vortex, the ellipticity angles of some areas, particularly in the outer middle region of the elliptic arc, are greater than 0°. However, these areas represent only a small portion. Thus, the value of this arc at the dimension of the ellipticity angle corresponds to a binary "0", which agrees with the design.

The optical field can be readily detected by illuminating the metasurface with a linearly polarized beam over a broadband spectrum, as demonstrated in the Supplementary Note 4. The SC-PVVB array can also propagate robust in free space, and simulated results can be found in Supplementary Note 7. This method offers a robust and straightforward approach for receivers to acquire the ciphertext (optical vector field). Owing to the high-dimensional capacity of a SC-PVVB across three distinct dimensions—morphology, polarization azimuth and ellipticity angle—the proposed encryption scheme is capable of securing the transmission of vast amounts of data with ultra-high security.

3 Discussion

We have successfully demonstrated a spatial-frequency patching metasurface to synthesize a novel VB called SC-PVVB, which is characterized by their ability to carry complex spatial morphology and polarization features. This is achieved through the superposition of two SC-PVBs in orthogonal CP states with a single geometric metasurface. The SC-PVVB exhibits a broadband response of intensity and polarization distribution across the wavelength spectrum ranging from 460 to 650 nm. The results are particularly notable for their implications in enhancing local control over the dimensions of optical beams, which supports a total of 13 channels by solely examining the morphology and polarization of the SC-PVVB. In our metasurface design, we use geometry phase to encode the vortex phase profile, which is only related to the rotation angle of the meta-structures. This enables a broadband response of vortex generation, requiring the meta-structures to function as half-waveplates. However, it should be noted that even with broadband phase response the diffraction efficiency drops off outside the operating wavelength. Generally, in order to ensure the phase modulation and enhance the efficiency, low-loss high-index dielectric materials are usually employed in structural design [55], including materials such as titanium dioxide (TiO_2), gallium nitride (GaN), indium tin oxide (ITO), and silicon nitride (SiN). As a proof of concept, we have utilized TiO_2 as the structural material in this paper. Additionally, TiO_2 is chemically and mechanically stable, making it suitable for various environmental conditions, including microfluidic applications [56]. Our proposed method can also be applied to on-chip devices [57]. By incorporating the phase of a Fourier transformer (FT) lens, the SC-PVVB can be generated on an arbitrary plane, which is highly suitable for chip application scenarios.

The spatial-frequency patching approach presented in this manuscript involves the integration of angular, radial, and lateral spatial-frequency components within the input field at the metasurface plane, which is totally different from Space Division Multiplexing (SDM) [58, 59]. SDM is a technique that amplifies the capacity of optical communication systems by enabling the transmission of multiple data streams along separate spatial paths. This can be achieved by dividing the space into distinct areas or by using various components like fiber bundles, multicore fibers, and few-mode fibers or relying on some spatial modes including VBs in free space [60–65], which provide distinct parallel channels for the simultaneous transmission of independent signals. We demonstrate the localized control of individual SC-PVVB' morphology, polarization ellipticity and azimuthal angles with spatial-frequency patching approach. The results indicate that the channel information is indeed spatially distributed. However, unlike the traditional OAM-based multiplexing, which relies on global manipulation and results in fewer channels within a single vortex beam, our method integrates different spatial-frequency components that interact with each other to generate a unified channels within a single vortex beam, thus enabling a super-capacity vortex beam with modulated morphology and polarization that has never been realized before.

The information capacity of a single SC-PVVB can be also improved furtherly. With each adjustable parameter capable of adopting M distinct values, this allows for M^{13} possible combinations, significantly surpassing the 5×5 combinations offered by previous work [1], which supported only two channels with five possible values each. In addition, the division of areas corresponding to each dimension of the SC-PVVB does not necessarily have to correspond strictly, which will further improve the information capacity and security. As shown in Eq. 1, the

polarization ellipticity angle distribution which is associated with the amplitude distributions of two circularly polarized SC-PVB can be completely modulated independently, demonstrating an unrestricted capacity with very loose binding conditions, compared with other two dimensions. Moreover, channels can be further improved with more segments involved. Theoretically, the proposed technique for generating a seamless and smooth ring can incorporate countless partial elliptical arcs, providing the tangent lines at each junction align perfectly, offering endless design possibilities.

Overall, the development of SC-PVVBs offers a high degree of complexity and controllability, which has the potential to revolutionize various fields in optics. The ability to locally control complex optical fields could lead to more secure optical communication systems, where information can be encoded with higher levels of capacity and security. The precise management of polarization and morphology could facilitate more sophisticated interactions with matter, potentially driving progress in fields such as quantum computing, optical trapping and biosensing.

4 Methods

4.1 Sample fabrication

The fabrication of the metasurface involves a sequence of electron beam lithography (EBL) and reactive ion etching (RIE) processes. Initially, a 600-nm-thick TiO_2 thin film is deposited onto a smooth glass (SiO_2) substrate via electron beam evaporation (EBE) due to its high material utilization, precise thickness control, and good compatibility with subsequent nano-fabrication processes [66]. High-energy electrons are directed at the TiO_2 in the crucible, causing it to evaporate and then deposit onto the glass substrate (see more details of the effects on TiO_2 deposition using electron beam evaporation in Ref. [67]). Following this, a layer of polymethyl methacrylate (PMMA) is applied to the TiO_2 thin film using spin coating. Subsequent to the EBL process, the PMMA resist is developed. A chromium (Cr) film is then deposited onto the PMMA pattern, again utilizing the EBE process. This is followed by the removal of the remaining PMMA resist. The TiO_2 pattern is subsequently etched using the RIE process. Finally, the Cr mask is removed through chemical etching.

4.2 Optical setup

The experimental optical setup for the metasurface is illustrated in Fig. 4a. The laser from a supercontinuum laser source (SC-PRO, Wuhan Yangtze Soton Laser Co., Ltd., 430 nm-2400 nm) filtered by an acousto-optic tunable filter (AOTF, Wuhan Yangtze Soton Laser Co., Ltd., 400 nm–2000 nm) is initially polarized by a polarizer (P1). The polarized beam is then mildly focused onto the metasurface using a lens (L1, $f=50$ mm). An aspheric lens (L2, $f=16$ mm) with a numerical aperture (NA) of 0.65 is placed obliquely behind the metasurface to execute a Fourier transform on the optical field in the metasurface plane. The optical field in the focal plane of L2 is transmitted to a scientific CMOS (sCMOS) camera (Dhyana 400BSI V2, Tucsen, China) via a 4-f system, which includes a pair of lenses (L3 and L4, not shown in the figure for simplicity). To analyze the polarization state of the SC-PVVB, a quarter-wave plate (QWP) and a second polarizer (P2) are strategically positioned in front of the sCMOS camera.

Supplementary Information

The online version contains supplementary material available at https://doi.org/10.1186/s43593-024-00077-3.

Additional file 1.

Acknowledgements

Q.S. acknowledges the funding support from the National Natural Science Foundation of China (No. 12204264), the Jiangsu Provincial Fundamental Research Program (No. BK20243029), the Shenzhen Science and Technology Innovation Commission (No. JCYJ20230807111706014). X.L. acknowledge financial support from the National Key R&D Program of China (2021YFB2802003), National Natural Science Foundation of China (NSFC) (62325503). P.L. acknowledges the funding support from the National Natural Science Foundation of China (81930048), the Guangdong Science and Technology Commission (2019BT02X105), Hong Kong Research Grant Council (15217721, C7074-21), and the Hong Kong Polytechnic University (P0045680, P0043485, P0045762, P0049101). Y.S. acknowledges the National Key Research and Development Program of China (No. 2023YFF0613600), the Shanghai Pilot Program for Basic Research, National Natural Science Foundation of China (No. 62205246), and Science and Technology Commission of Shanghai Municipality (No. 22ZR1432400).

Author contributions

Z. Y. and Q. S. conceived the idea; Z. Y. conducted the numerical computation and experiment and prepared the figures; X. G. conducted the numerical computation of the metasurface; J. Y., Z. W., T. Z., Y. S. and B. L. assisted in building up the system and prepare the figures; Z. Y., X. L. and Q. S. wrote the manuscript. P. L., X. L. and Q. S. supervised the project. All members contributed to the discussion of the results and proofreading of the manuscript.

Availability of data and materials

The data and code that support the figures and other findings of this study are available from the corresponding authors upon reasonable request.

Declarations

Competing interests

The authors declare no competing interests.

Received: 1 June 2024 Revised: 27 September 2024 Accepted: 7 October 2024
Published online: 02 December 2024

References

1. M. Liu et al., Broadband generation of perfect poincaré beams via dielectric spin-multiplexed metasurface. Nat. Commun. **12**, 2230 (2021)
2. Y. Bao, J. Ni, C.W. Qiu, A minimalist single layer metasurface for arbitrary and full control of vector vortex beams. Adv. Mater. **32**, 1905659 (2020)
3. P. Li et al., Generation of perfect vectorial vortex beams. Opt. Lett. **41**, 2205–2208 (2016)
4. Y. Liu et al., Generation of perfect vortex and vector beams based on pancharatnam-berry phase elements. Sci. Rep. **7**, 44096 (2017)
5. D. Li, S. Feng, S. Nie, C. Chang, J. Ma, C. Yuan, Generation of arbitrary perfect poincaré beams. J. Appl. Phys. **125**, 073105 (2019)
6. R. Xu et al., Perfect higher-order poincaré sphere beams from digitalized geometric phases. Phys. Rev. Appl. **10**, 034061 (2018)
7. L. Li et al., High efficiency generation of tunable ellipse perfect vector beams. Photonics Res. **6**, 1116–1123 (2018)
8. C. Wan, A. Chong, Q. Zhan, Optical spatiotemporal vortices. eLight **3**, 11 (2023). https://doi.org/10.1186/s43593-023-00042-6
9. H. Chen, Q. Wang, X. Liu et al., 100-W Yb:YAG thin-disk vortex laser oscillator. Light Adv. Manuf. **4**, 38 (2023). https://doi.org/10.37188/lam.2023.040
10. M. Chen, M. Mazilu, Y. Arita, E.M. Wright, K. Dholakia, Dynamics of microparticles trapped in a perfect vortex beam. Opt. Lett. **38**, 4919–4922 (2013)
11. H. Qin et al., Exploiting extraordinary topological optical forces at bound states in the continuum. Sci. Adv. **8**, eade7556 (2022)
12. Y. Shi et al., Advances In light transverse momenta and optical lateral forces. Adv. Opt. Photonics **15**, 835–906 (2023)
13. Y. Shi et al., Optical manipulation with metamaterial structures. Appl. Phys. Rev. **9**, 031303 (2022)
14. M. Wang, G., Hu, S., Chand et al., Spin-orbit-locked hyperbolic polariton vortices carrying reconfigurable topological charges. eLight **2**, 12 (2022). https://doi.org/10.1186/s43593-022-00018-y
15. C. Zhang, C. Min, L. Du, X.-C. Yuan, Perfect optical vortex enhanced surface plasmon excitation for plasmonic structured illumination microscopy imaging. Appl. Phys. Lett. **108**, 201601 (2016)
16. R. Zheng et al., Active multiband varifocal metalenses based on orbital angular momentum division multiplexing. Nat. Commun. **13**, 4292 (2022)
17. H. Ren, X. Fang, J. Jang, J. Bürger, J. Rho, S.A. Maier, Complex-amplitude metasurface-based orbital angular momentum holography in momentum space. Nat. Nanotechnol. **15**, 948–955 (2020)
18. H. Ren et al., Metasurface orbital angular momentum holography. Nat. Commun. **10**, 2986 (2019)
19. S. So et al., Multicolor and 3D holography generated by inverse-designed single-cell metasurfaces. Adv. Mater. **35**, 2208520 (2023)
20. T. Naeem et al., Dynamic chiral metasurfaces for broadband phase-gradient holographic displays. Adv. Opt. Mater. **11**, 2202278 (2023)
21. P. Georgi et al., Optical secret sharing with cascaded metasurface holography. Sci. Adv. **7**, Eabf9718 (2021)
22. S. Latif et al., Spin-selective angular dispersion control in dielectric metasurfaces for multichannel meta-holographic displays. Nano Lett. **24**, 708–714 (2024)
23. H. Zhou et al., Polarization-encrypted orbital angular momentum multiplexed metasurface holography. ACS Nano **14**, 5553–5559 (2020)
24. V. Nikolay, S. Bogdan, S. Maksim et al., Design of broadband terahertz vector and vortex beams: II. Holographic assessment. Light Adv. Manuf. **3**, 44 (2022). https://doi.org/10.37188/lam.2022.044
25. V. Nikolay, S. Bogdan, S. Maksim et al., Design of broadband terahertz vector and vortex beams: I. Review of materials and components. Light Adv. Manuf. **3**, 54 (2022). https://doi.org/10.37188/lam.2022.043
26. F. Zhu et al., Free-space optical communication link using perfect vortex beams carrying orbital angular momentum (Oam). Optics Communications **396**, 50–57 (2017)
27. H. Tan et al., A free-space orbital angular momentum multiplexing communication system based on a metasurface. Laser Photonics Rev. **13**, 1800278 (2019)
28. H. Ren, X. Li, Q. Zhang, M. Gu, On-chip noninterference angular momentum multiplexing of broadband light. Science **352**, 805–809 (2016)
29. M. Mq et al., Single-cell-driven tri-channel encryption meta-displays. Adv. Sci. **9**, 2203962 (2022)
30. J. Kim et al., Photonic encryption platform via dual-band vectorial metaholograms in the ultraviolet and visible. ACS Nano **16**, 3546–3553 (2022)
31. X. Ouyang et al., Synthetic helical dichroism for six-dimensional optical orbital angular momentum multiplexing. Nat. Photonics **15**, 901–907 (2021)
32. J. Hou, G. Situ, Image encryption using spatial nonlinear optics. eLight. **2**, 3 (2022). https://doi.org/10.1186/s43593-021-00010-y
33. Q. Song, X. Liu, C.-W. Qiu, P. Genevet, Vectorial metasurface holography. Appl. Phys. Rev. **9**, 011311 (2022)
34. Q. Song et al., Broadband decoupling of intensity and polarization with vectorial fourier metasurfaces. Nat. Commun. **12**, 3631 (2021)
35. Q. Song et al., Ptychography retrieval of fully polarized holograms from geometric-phase metasurfaces. Nat. Commun. **11**, 2651 (2020)
36. J.P. Balthasar Mueller, N.A. Rubin, R.C. Devlin, B. Groever, F. Capasso, Metasurface polarization optics: independent phase control of arbitrary orthogonal states of polarization. Phys. Rev. Lett. **118**, 113901 (2017)
37. M. Liu et al., Multifunctional metasurfaces enabled by simultaneous and independent control of phase and amplitude for orthogonal polarization states. Light Sci. Appl. **10**, 107 (2021)
38. Q. Song, M. Odeh, J. Zúñiga-Pérez, B. Kanté, P. Genevet, Plasmonic topological metasurface by encircling an exceptional point. Science **373**, 1133–1137 (2021)
39. O. Ac et al., Dielectric metasurfaces for complete and independent control of the optical amplitude and phase. Light Sci. Appl. **8**, 92 (2019)
40. B. Xiong et al., Breaking the limitation of polarization multiplexing in optical metasurfaces with engineered noise. Science **379**, 294–299 (2023)
41. D. Zl et al., Vectorial compound metapixels for arbitrary nonorthogonal polarization steganography. Adv. Mater. **33**, 2103472 (2021)
42. S. Schulz et al., Roadmap on photonic metasurfaces. Appl. Phy. Lett. **124**, 260701 (2024). https://doi.org/10.1063/5.0204694
43. F. Mei et al., Cascaded metasurfaces for high-purity vortex generation. Nat. Commun. **14**, 6410 (2023)
44. E. Karimi, S.A. Schulz, I. De Leon, H. Qassim, J. Upham, R.W. Boyd, Generating optical orbital angular momentum at visible wavelengths using a plasmonic metasurface. Light Sci. Appl. **3**, E167 (2014)
45. F. Yue, D. Wen, J. Xin, Bd. Gerardot, J. Li, X. Chen, Vector vortex beam generation with a single plasmonic metasurface. Acs Photonics **3**, 1558–1563 (2016)
46. Zh. Jiang et al., A single noninterleaved metasurface for high-capacity and flexible mode multiplexing of higher-order poincaré sphere beams. Adv. Mater. **32**, 1903983 (2020)
47. J. Ni et al., Multidimensional phase singularities in nanophotonics. Science **374**, Eabj0039 (2021)
48. Q. Zhou et al., Generation of perfect vortex beams by dielectric geometric metasurface for visible light. Laser Photonics Rev. **15**, 2100390 (2021)
49. Q. Yang et al., Ultra-secure optical encryption based on tightly focused perfect optical vortex beams. Nanophotonics **11**, 1063–1070 (2022)
50. H. Ahmed et al., Multichannel superposition of grafted perfect vortex beams. Adv. Mater. **34**, E2203044 (2022)
51. Y. Zhang, W. Liu, J. Gao, X. Yang, Generating focused 3D perfect vortex beams by plasmonic metasurfaces. Adv. Opt. Mater. **6**, 1701228 (2018)
52. H. Zhang et al., Grafted optical vortex with controllable orbital angular momentum distribution. Opt. Express **27**, 22930–22938 (2019)
53. H. Ahmed, M.A. Ansari, Y. Li, T. Zentgraf, M.Q. Mehmood, X. Chen, Dynamic control of hybrid grafted perfect vector vortex beams. Nat. Commun. **14**, 3915 (2023)
54. Y. Shen, X. Yang, D. Naidoo, X. Fu, A. Forbes, Structured ray-wave vector vortex beams in multiple degrees of freedom from a laser. Optica **7**, 820–831 (2020)
55. S. Colburn et al., Broadband transparent and cmos-compatible flat optics with silicon nitride metasurfaces [invited]. Opt. Mater. Express **8**, 2330–2344 (2018)
56. S. Sun et al., Real-time tunable colors from microfluidic reconfigurable all-dielectric metasurfaces. ACS Nano **12**, 2151–2159 (2018)
57. J. Ni et al., Unidirectional unpolarized luminescence emission via vortex excitation. Nat. Photonics **17**, 601–606 (2023)
58. R. Dj, F. Jm, N. Le, Space-division multiplexing in optical fibres. Nat. Photonics **7**, 354–362 (2013)
59. Z. Wan, Y. Shen, Z. Wang, Z. Shi, Q. Liu, X. Fu, Divergence-degenerate spatial multiplexing towards future ultrahigh capacity, low error-rate optical communications. Light Sci. Appl. **11**, 144 (2022)
60. A.E. Willner, K. Pang, H. Song, K. Zou, H. Zhou, Orbital angular momentum of light for communications. Appl Phys Rev. **8**, 41312 (2021)

61. N. Bozinovic et al., Terabit-scale orbital angular momentum mode division multiplexing in fibers. Science **340**, 1545–1548 (2013)
62. A. Trichili, K.H. Park, M. Zghal, B.S. Ooi, M.S. Alouini, Communicating using spatial mode multiplexing: potentials, challenges and perspectives. . IEEE Commun. Surv. Tutor. **21**, 3175–3203 (2019)
63. G. Li, N. Bai, N. Zhao, C. Xia, Space-division multiplexing: the next frontier in optical communication. Adv. Opt. Photonics **6**, 413–487 (2014)
64. J. Wang et al., Terabit free-space data transmission employing orbital angular momentum multiplexing. Nat. Photonics **6**, 488–496 (2012)
65. T. Lei et al., Massive individual orbital angular momentum channels for multiplexing enabled by dammann gratings. Light Sci. Appl. **4**, E257–E257 (2015)
66. S. Sun et al., All-dielectric full-color printing with Tio2 metasurfaces. ACS Nano **11**, 4445–4452 (2017)
67. V. Mikhelashvili, G. Eisenstein, Effects of annealing conditions on optical and electrical characteristics of titanium dioxide films deposited by electron beam evaporation. J. Appl. Phys. **89**, 3256–3269 (2001)